Structural and Thermal Analysis of Lipid Vesicles Encapsulating Hydrophobic Gold Nanoparticles

Gregory Von White, II,[†] Yanjing Chen,[‡] Julia Roder-Hanna,[‡] Geoffrey D. Bothun,[‡,*] and Christopher L. Kitchens[†,*]

[†]Department of Chemical and Biomolecular Engineering, Clemson University, Clemson, South Carolina 29634, United States and [‡]Department of Chemical Engineering, University of Rhode Island, Kingston, Rhode Island 02881, United States

ABSTRACT

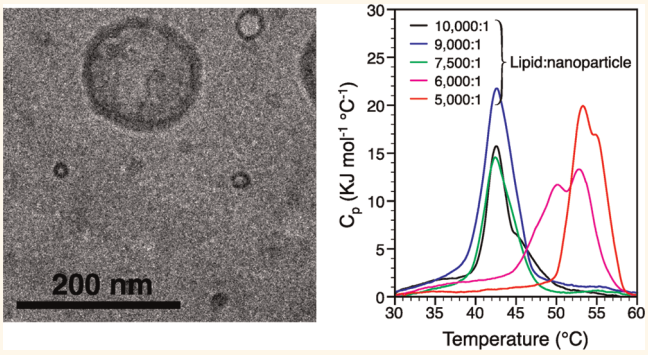

The structure and stability of hybrid lipid vesicles containing bilayer-encapsulated hydrophobic nanoparticles is dependent upon lipid phase behavior. By embedding stearylamine-stabilized gold nanoparticles in dipalmitoylphosphatidylcholine/dipalmitoylphosphatidylglycerol vesicles, we show that encapsulation at lipid to nanoparticle ratios from 10 000:1 to 5000:1 leads to bilayer thickening and hydrophobic mismatch, favoring nanoparticle inclusion in gel phase vesicles. High loadings lead to large increases in the gel to fluid melting temperature upon heating and significant hysteresis on cooling, which cannot be attributed solely to excess free ligand. This behavior is due to a cooperative effect of excess free SA ligand and nanoparticle embedment. Nanoparticle clustering was observed during lipid melting and could be reversed upon lipid freezing owing to lateral capillary forces within the bilayer. The impact of nanoparticle embedment on vesicle structure and properties at such low concentrations is reminiscent of hydrophobic proteins, suggesting that the underlying lipid biophysics between proteins and nanoparticle are similar and may provide a predictive design tool for therapeutic applications.

KEYWORDS: gold nanoparticle · vesicle · liposome · lipid phase behavior · domain formation

Significant advances in metal nanoparticle synthesis have afforded facile control of size, shape, and surface chemistry.[1−7] The biomedical field has greatly benefited by these advances, which has resulted in nanoparticle applications as contrast agents, hyperthermia agents, and targeted drug delivery devices.[8−13] Tailoring nanoparticle surface chemistry can be used to increase stability and bioavailability, decrease macrophage uptake, and enable site-specific targeting.[13−16]

Coating or encapsulating nanoparticles with lipids is a useful noncovalent approach to increase biocompatibility, as the stabilizing surface chemistry is similar to the structural components of the cellular membrane.[14,17−21] Hybrid lipid vesicle−nanoparticle systems are particularly attractive because they afford the potential use of hydrophobically stabilized nanoparticles in biomedical applications, such as triggered drug delivery.[17,18,22−25] Prior studies have demonstrated successful encapsulation of hydrophobically stabilized nanoparticles into lipid vesicles by embedding them in the hydrophobic acyl core of the bilayer (Figure 1).[19,26] Disruption of lipid ordering (fluidity of the membrane) and variations in lipid phase behavior, namely, lipid melting from a gel to fluid phase, has been observed with the incorporation of hydrophobic nanoparticles.

Park *et al.* encapsulated 3 to 4 nm stearylamine-stabilized gold nanoparticles (GNPs) into the hydrophobic bilayer of zwitterionic dimyristoylphosphatidylcholine (DPPC) vesicles and showed that increasing nanoparticle loading within the bilayer resulted in an increased membrane fluidity (or decrease lipid ordering).[19] The opposite effect has been observed by Chen *et al.* for 5 nm oleic acid stabilized maghemite particles in DPPC vesicles. In this case the nanoparticles increased lipid melting temperatures, which points to an increase in lipid ordering and stabilization of the bilayer against spontaneous leakage.[17] Most recently, Rasch *et al.* demonstrated uniform encapsulation of 1.9 nm diameter dodecanethiol-stabilized GNPs into egg phosphatidylcholine vesicles.[14] They concluded that the nanoparticles clustered within the fluid bilayers to yield a mixture of vesicles containing densely packed nanoparticles and vesicles void of nanoparticles. Under certain

* Address correspondence to bothun@egr.uri.edu; ckitche@clemson.edu.

Received for review October 31, 2011 and accepted May 26, 2012.

Published online May 26, 2012
10.1021/nn2042016

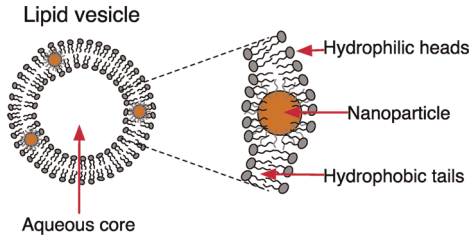

Figure 1. Schematic of a lipid vesicle encapsulating hydrophobic nanoparticles within the bilayer.

conditions Janus vesicles were observed due to GNP clustering. Collectively, these studies indicate that nanoparticle size impacts nanoparticle ordering within the bilayers and vesicle structure.[14] Investigating the effects of size, shape, and extent of nanoparticle loading on bilayer thickness, fluidity, and phase transitions is critical for the development of effective vesicle–nanoparticle assembly based therapies. Also critical is determining how ligand chemistry and the presence of excess ligand, as a result of preparation or desorption, impact vesicle–nanoparticle assembly and influence these properties.

Hydrophobic nanoparticle encapsulation within lipid bilayers resembles that of embedded transmembrane or hydrophobic proteins. In both cases the size of the hydrophobic region can exceed that of the bilayer thickness and result in "positive" hydrophobic mismatch. Hydrophobic mismatch, defined as the difference in hydrophobic thickness of the inclusion minus that of the bilayer, affects lipid ordering and phase behavior.[27−30] It also can lead to protein aggregation in an effort to minimize hydrophobic mismatch.[29,31] When mismatch is "positive", the hydrophobic inclusion will prefer to reside in the gel phase where the lipid tails are extended in an all-trans, unmelted state. Upon lipid melting (gel to fluid transition), greater positive hydrophobic mismatch arising from the fluid phase can lead to aggregation of the inclusions within the membrane.[32] While the analogy between embedded nanoparticles and proteins is intuitive, it has not been investigated in-depth. Furthermore, there are few studies that have examined the use of ordered gel phase vesicles rather than disordered fluid phase vesicles for nanoparticle encapsulation. Gel phase vesicles offer a thicker hydrophobic bilayer and a greater resistance to membrane bending or compression.

To address these areas, we have employed small-angle neutron scattering (SANS), differential scanning calorimetry (DSC), and cryogenic transmission electron microscopy (cryo-TEM) to determine the effects of nanoparticle concentration, expressed as the number ratio of lipid molecules to nanoparticles (*L*/*N*), and temperature on vesicles composed of DPPC and anionic dipalmitoylphosphatidylglycerol (DPPG) at a molar ratio of 85:15. SANS has recently been used to examine vesicle bilayer thickness with encapsulated pristine C_{60} fullerene[33] and ∼8 nm hydrophobic iron oxide

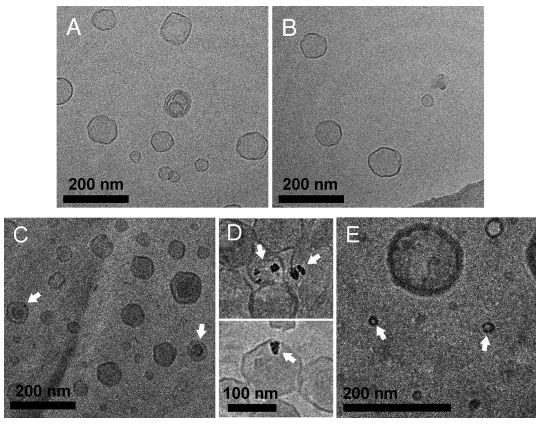

Figure 2. Representative cryo-TEM micrographs of (A, B) DPPC/DPPG vesicles and (C, D, E) DPPC/DPPG vesicles with embedded GNPs at *L*/*N* = 5000:1. The scale bar in D is common to both images. White arrows denote embedded GNPs.

TABLE 1. Bilayer Thickness Determined from SANS for Varying Lipid Vesicle Systems at Varying Temperatures and Nanoparticle Loadings

		Kratky–Porod	lamellar model		
		t_b^i (Å)	t_b^i (Å)	σ (Å)	PDI
DPPC/DPPG vesicles	25 °C	42	43.8	6.8	0.16
	37 °C	43	43.6	7.3	0.17
	50 °C	43	40.2	10.2	0.25
10 000:1 *L*/*N*	25 °C	45	44.2	7.2	0.16
	37 °C	45	43.9	7.3	0.17
	50 °C	43	40.0	12.0	0.30
5000:1 *L*/*N*	25 °C	45	44.9	8.8	0.20
	37 °C	45	44.2	7.9	0.18
	50 °C	44	39.9	1.9	0.05

particles.[23] In this work, we employed gold nanoparticles that were prepared in water using a citrate-based synthesis, similar to Jana *et al.*[34] The GNPs were resuspended in toluene after exchanging the citrate with stearylamine (SA) ligands.[35,36] The SA-stabilized GNPs were purified by three replicates of ethanol antisolvent precipitation, centrifugation, and redispersion in neat toluene with sonication. Size fractionation was achieved by recovering the GNPs that precipitate with centrifugation between 40% and 45% ethanol antisolvent by volume. This process yielded hydrophobic GNPs with an average core diameter of 3.9 ± 0.8 nm (Figure S1). Vesicle encapsulation of the GNPs was performed using thin film hydration. Details of the experimental methods are provided in the Supporting Information.

RESULTS AND DISCUSSION

Cryogenic transmission microscopy was first conducted at 25 °C and the highest GNP loading, *L*/*N* = 5000:1, to verify GNP loading within the vesicles. This *L*/*N* ratio of 5000:1 provided 20 GNPs per 100 000 lipid molecules, which is approximately equivalent to the

TABLE 2. DPPC/DPPG Lipid Pretransition (T_p) and Melting Transition (T_m) with SA or GNPs (SA-coated)

lipid−SA vesicles			lipid−GNP vesicles		
SA (mol %)	T_p (°C)	T_m (°C)	L/N[b]	T_p (°C)	T_m (°C)
0	34.5	41.5	10 000:1	35.9	42.5
1	37.3	42.4	9000:1		42.7
2	37.3	42.6	7500:1		42.5
5	37.8	42.6, 45.6	6000:1		50.2, 52.9
10	38.3	42.6, 45.8	5000:1		53.3, 54.8
20[a]		56.2			
30[a]		59.5			
50		60.5			

[a] Approximated T_m based on broad melting peaks. [b] Estimated total SA concentrations from 41.2 to 58.3 mol % (lipid basis) with increasing L/N.

number of lipids in a 100 nm diameter vesicle. Bare vesicles were primarily unilamellar with diameters near 100 nm (Figure 2A, B). The bilayers are clearly visible, while the vesicle interiors exhibit similar contrast to the bulk phase. GNP−vesicles were also unilamellar and similar in size, with embedded GNPs visible at the expected GNP per vesicle ratio given that nanoparticles out of the focus plane are not easily observed (Figure 2C, D). Small GNP−vesicles were also observed (~25 nm in diameter), and these vesicles appear to contain embedded GNPs (Figure 2E).

SANS experiments were performed at temperatures corresponding to the tilted gel (25 °C), rippled gel (37 °C), and fluid phases (50 °C) of DPPC/DPPG vesicles and at nanoparticle loadings of L/N of 10 000:1 and 5000:1. DPPC/DPPG phase transition temperatures are listed in Table 2. Kratky−Porod analysis of the radial averaged SANS intensity as a function of the scattering vector, $I(q)$, was performed to determine the vesicle radius of gyration, R_g, shown in Table 1. The Kratky−Porod method provides bilayer thicknesses that are comparable to published values[37] and suggests subtle increases in the bilayer thickness with nanoparticle and stearylamine ligand inclusion, particularly at temperatures corresponding to fluid phases (25 and 37 °C).

To elucidate bilayer thicknesses to a greater precision, further analysis of the SANS data required fitting the scattering intensity to a dilute lamellar form factor using eqs 1 and 2.[37−40]

$$I(q) = \frac{2\pi P(q)}{t_b^i q^2} \quad (1)$$

$$P(q) = \frac{2(\mathrm{SLD}_{solv} - \mathrm{SLD}_b)^2}{q^2}[1 - \cos(qt_b^i)e^{-q^2\sigma^2/2}] \quad (2)$$

where the form factor $P(q)$ is a function of the solvent and bilayer scattering length densities (SLD_{solv} and SLD_b) and the variation in bilayer thickness (σ), which is attributed to polydispersity. In the data fitting, the bilayer thickness (t_b^i, where i denotes the gel (g) or fluid (f) phases) and thickness variation (σ) were set as adjustable parameters, while the SLD_{solv} for deuterium oxide and SLD_b for the hydrogenated phospholipid bilayers were held at 6.33×10^{-6} and -2.77×10^{-7} Å^{-2}, respectively. Results from the fitted parameters are in Table 1.

Figure 3 shows plots of the experimental SANS $I(q)$ fit with the lamellar form factor model. On the basis of the SANS spectra, the bare vesicles were on the order of 100 nm in diameter, as compared to the GNP−vesicles at L/N ratios of 10 000:1 and 5000:1, which were greater than 120 nm in diameter. The exact diameter could not be determined with great accuracy due to the polydispersity of vesicles in solution (decreasing intensity with increasing q is evident at the low q range in place of the expected Guinier regions); however, the vesicle size and polydispersity demonstrated an increasing trend with increasing nanoparticle loading. There was no evidence of micelles or nanoparticle aggregates, which is consistent with cryo-TEM results.

As expected, bilayer thickness decreased with increasing temperature for the bare vesicles, from $t_b^g = 43.8 \pm 6.8$ Å at 25 °C to $t_b^f = 40.2 \pm 10.2$ Å at 50 °C. These thicknesses and changes agree well with literature values for the gel to fluid phase transition.[37] With GNPs, the bilayer thickness is again greater at 25 and 37 °C and increases with increasing GNP and SA loading. This suggests the presence of nanoparticles and/or excess SA ligand induced ordered gel phases. In contrast, t_b^f at 50 °C suggests minimal effect on bilayer thickness in the fluid phase. Variations in σ were determined with the lamellar model, and the polydispersity differed with values up to 0.30; however, no clear trends were observed and sensitivity analysis places little weight on this value. Previous studies have simply assumed a σ value of $t_b^i/4$, or a polydispersity of 25%.[38]

Changes in bilayer thickness can be attributed to mismatch between the hydrophobic bilayer thickness and the diameter of the GNPs. Hydrophobic mismatch, even for low inclusion concentrations, can have significant effects on lipid order.[29] DSC was conducted to determine the effects of GNP loading and free SA ligand on lipid phase behavior. Results are presented first for lipid−SA vesicles (no GNPs), where vesicles were prepared from dry films of lipid + SA at SA concentrations from 0 to 50 mol % (Figure 4A). DPPC/DPPG vesicles exhibited a gel to rippled gel pretransition (T_p) at 35.5 °C and a rippled gel to fluid melting transition (T_m) at 41.5 °C. T_p and T_m increased with increasing SA concentration (Table 2). Single melting peaks were observed at 1 and 2 mol % SA, but a clear shoulder peak becomes evident above 2 mol %, denoting phase separation, which is apparent at 5 and 10 mol % SA in the observed dual peaks. For 20 mol % SA and above, the vesicles exhibited broad melting peaks at higher temperatures with low melting enthalpy. Minimal melting hysteresis was observed at

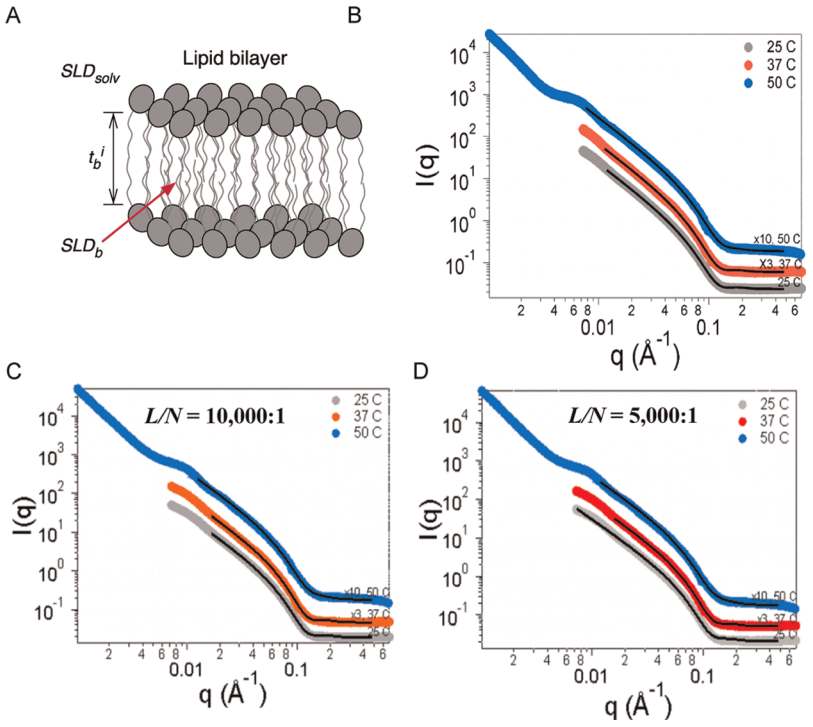

Figure 3. (A) Schematic of the lamellar model used for SANS data analysis. (B–D) SANS spectra fit with a lamellar model for (B) DPPC/DPPG vesicles (~100 nm in diameter) and DPPC/DPPG vesicles dispersed in deuterium oxide at 25, 37, and 50 °C with 3.9 nm GNPs partitioned into the bilayer at *L*/*N* of (C) 10 000:1 and (D) 5000:1.

all SA concentrations. Changes in DPPC/DPPG phase behavior due to SA can be attributed to electrostatic headgroup interactions. First, repulsion between the cationic SA amine and the terminal positive choline group of DPPC restricted the lipid headgroup dipole reorientation, from perpendicular (gel) to parallel (fluid) to the membrane/water interface, that accompanies melting. This effect is analogous to that of cationic lipids mixed with DPPC.[41,42] Second, attraction between SA and anionic DPPG led to phase separation and increased lipid ordering. The fact that a pretransition was observed for SA concentrations less than 20 mol % shows that SA did not prevent lipid tilt in the gel phase.

In GNP-loaded vesicles a pretransition shoulder was observed at the lowest GNP loading, but disappeared at higher loadings (Figure 4B). There was also a clear increase in T_m at all loadings relative to bare vesicles. At *L*/*N* ratios above 7500:1 the increase in T_m was small and shoulder peaks were observed near 45 °C, consistent with phase separation. At higher loadings (*L*/*N* ratios <7500:1) clear phase separation was observed and there was a significant increase in T_m. These results suggest that "low" and "high" degrees of encapsulation exhibit different effects on lipid phase behavior. To explore this further, melting hysteresis was examined at the lowest and highest nanoparticle loading (Figure 4C). At a *L*/*N* ratio of 10 000:1 there was little difference in the primary lipid melting peak with heating and cooling; however, some hysteresis was observed in the shoulder. At *L*/*N* = 5000:1 hysteresis was significant and the difference between the melting onset temperatures for heating and cooling was ~7 °C. The hysteresis was reversible, as evident from the consistent melting peaks observed with heating (Figure 4D).

The effect of GNPs on phase behavior was not unlike that of SA, where concentrations of 5 mol % and higher led to clear phase separation with high T_m peaks. Hence, there is an apparent cooperative effect of SA and GNPs on lipid phase behavior. To elucidate the effects of SA in GNP vesicles, excess SA (despite washing) and SA ligand density on the GNPs was determined by thermogravametric analysis (TGA; Figure S2). TGA results suggest that the excess SA concentration was on the order of 7000 molecules per GNP and that the SA ligand concentration was 5.8 nm^{-2}. Clearly the ethanol washing technique employed was inefficient in removing excess SA (see the Supporting Information for further discussion).[43,44] On the basis of the excess SA concentration, which corresponds to a range from 41 to 58 mol %, the observed phase behavior cannot be attributed to the nanoparticles alone. The SA excess could explain lipid phase separation and increases in T_m at high nanoparticle loadings (*L*/*N* > 7500:1), but it does not explain why high and low loadings exhibit markedly different phase behavior and significant T_m hysteresis.

At this point two questions arise: Why do "low" and "high" nanoparticle loadings have different effects on

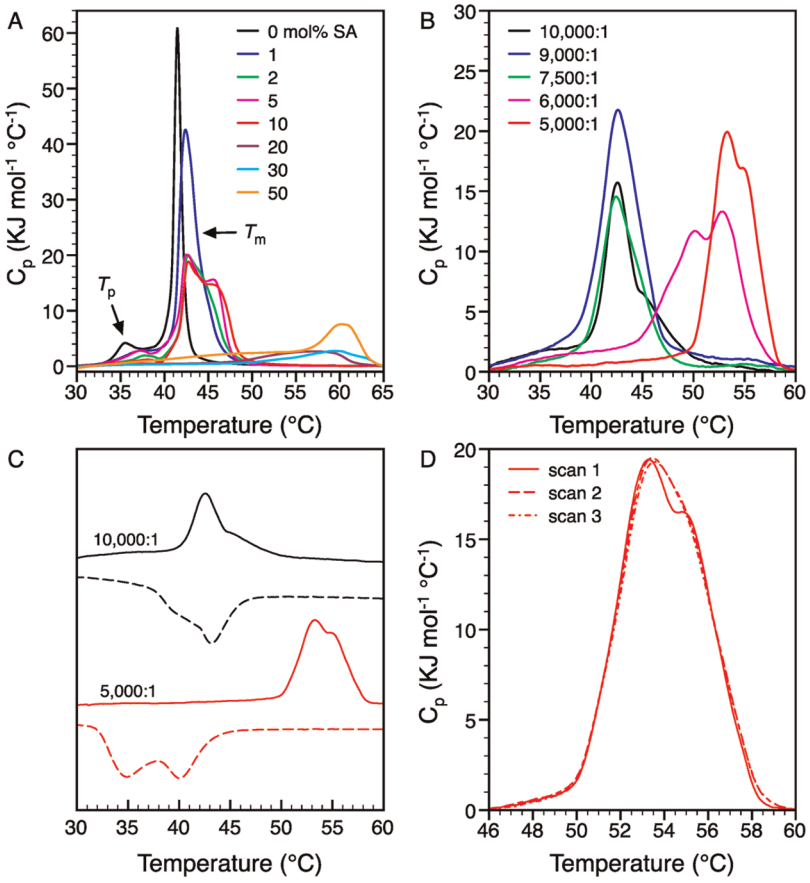

Figure 4. DSC thermographs of (A) DPPC/DPPC vesicles (inset) as a function of SA concentration (membrane basis) and (B) gold nanoparticle-loaded DPPC/DPPG vesicles as a function of *L*/*N*. For A and B the scans are from the first heating cycle. (C) Melting hysteresis from heating (solid lines) and cooling (dashed lines) scans of DPPC/DPPG vesicles at *L*/*N* = 10 000:1 and 5000:1. (D) Three consecutive heating scans at *L*/*N* = 5000:1. All heating and cooling scans were performed at 1 °C min^{-1}.

lipid melting, and what is the cause for melting hysteresis? DSC results suggest that this cannot be solely attributed to excess SA. To address these questions, a model has been employed that has been used for hydrophobic proteins. The interaction energy, $\Delta\Omega$, between hydrophobic GNP inclusions due to lateral capillary forces within a membrane was calculated as[45]

$$\Delta\Omega(L) = 2\pi d_p q(\sigma_0 - k_{c,i}q^2)\left(\frac{d_p - l_i}{2}\right)^2\left[\frac{K_1(qd_p/2) - qrK_0(qL)/2}{K_0(qd_p/2) + K_0(qL)} - \frac{K_1(qd_p/2)}{K_0(qd_p/2)}\right] \quad (3)$$

where L is the center-to-center nanoparticle separation distance, q is the capillary length, σ_0 is the membrane surface tension, and K_0 and K_1 are modified Bessel functions of the zero and first order, respectively. Values for q and σ_0 were taken from Kralchevsky *et al.*[45] The terms $k_{c,i}$ and l_i are the membrane bending modulus and hydrophobic thickness, respectively, and the subscript i denotes the gel or fluid phase. Values of 10^{-18} J were used for $k_{c,i}$ in the gel phase and 10^{-19} J for $k_{c,i}$ in the fluid phase.[46] The term $(d_p - l_i)/2$ represents hydrophobic mismatch. This model is based on the existence of a three-phase contact angle existing between water, lipid, and the inclusion (*i.e.*, the embedded GNPs are exposed to water; Figure 5B).

Results for $\Delta\Omega$ shown in Figure 5A indicate that a repulsive force exists between embedded nanoparticles at lower temperatures where the lipids exist in the gel phase ($k_{c,g}q^2 > \sigma_0$), while attractive forces are predominant at higher temperatures, where the lipids exist in the fluid phase ($k_{c,f}q^2 < \sigma_0$). The repulsive or attractive forces increase with increasing nanoparticle diameter. On the basis of this model, encapsulated nanoparticles can cluster upon lipid melting (gel to fluid, schematic shown in Figure 5B), and this clustering is more prominent at larger nanoparticle diameters. Analyzing van der Waals attraction between two nanoparticles (calculations based on GNPs used in this work) within the bilayer shows that the lateral capillary forces are longer ranged than vdW forces and that only at short separation distances ($L/d_p \approx 1$) would the particles irreversibly aggregate. However, the presence of ligands would prevent these distances from being reached *via* steric repulsion. This analysis suggests that reversible clustering *via* lateral capillary forces is plausible for vesicle−nanoparticle assemblies where the bilayer hydrophobic thickness is close to that of the nanoparticle diameter.

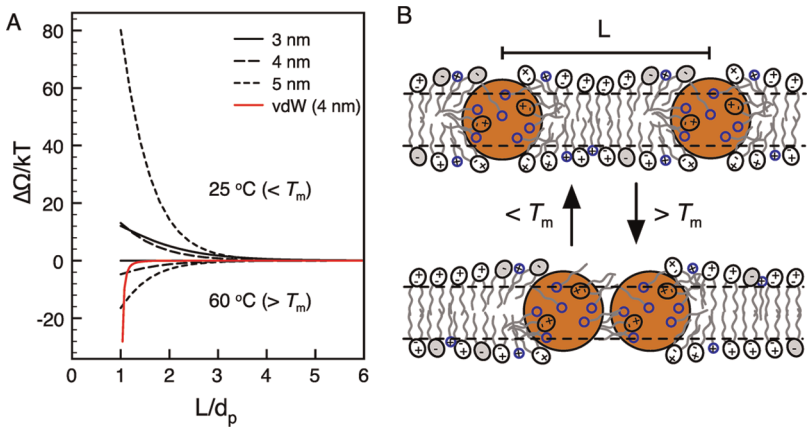

Figure 5. (A) Calculated increases in DPPC/DPPG bilayer thickness as a function of the lipid to nanoparticle ratio and the stearylamine coating thickness at 25 °C. The thickness of the DPPC/DPPG vesicles (no nanoparticles) was based on SANS. Increases in bilayer thickness are based on SANS experiments.

CONCLUSIONS

Even with the significant effects of free SA ligand on lipid phase behavior, our results suggest that the GNPs were dispersed in gel vesicles, but clustered in fluid vesicles. This is supported by SANS results, where gel bilayers thickened and fluid bilayers thinned. Clustering has been observed by Rasch *et al.*[14] for dodecanethiol-coated GNPs in fluid egg PC bilayers. In their case the GNP core diameters were smaller, 1.9 nm, and the loadings were higher, up to L/N = 1500:1. Our analysis suggests that similar behavior is observed with larger GNPs despite the additional elastic energy needed to distort the bilayers. This appears to be driven in part by SA desorption from the GNP surface and possibly aided by the presence of free SA ligand. Clustering upon melting is driven by greater hydrophobic mismatch between GNPs in the fluid phase relative to the gel phase coupled with lipid-mediated forces driven by lateral capillarity. These forces are attractive in the fluid phase, but repulsive in the gel phase due to the order of magnitude difference in bending moduli. We summarize our results as follows:

(I) At $L/N \geq$ 7500:1 moderate bilayer thickening was observed, suggesting increased lipid ordering. This is reinforced by the disappearance of the ripple gel pretransition and the appearance of a shoulder in the primary melting endotherm. Slight melting hysteresis was observed in the melting endotherm, demonstrating an onset of phase segregation. These results indicate that, for the given experimental conditions, the GNPs remained dispersed within gel or fluid bilayers at low nanoparticle loadings.

(II) At $L/N <$ 7500:1 bilayer thickening was observed, as well as a significant increase in T_m and pronounced melting hysteresis. Our observation that GNP clusters existed at high loadings may reflect dynamic restructuring driven by the extension of the stearylamine coating and lateral capillary forces. Consistent thermographs across multiple heat/cool (melt/freeze) cycles indicate that this was a reversible process. Furthermore, the unique phase behavior of the nanoparticle-loaded vesicle cannot be attributed solely to the excess stearylamine.

The present work demonstrates the effects that encapsulated hydrophobic nanoparticles can have on the structure and phase behavior of hybrid lipid vesicles. A better understanding of these properties will aid the design of nanoparticle-loaded vesicles for therapeutic applications. The fact that protein models may be applicable to these structures suggests that the underlying lipid biophysics between proteins and nanoparticle is similar and may provide a predictive design tool.

EXPERIMENTAL METHODS

Materials. The metal precursor hydrogen tetrachloroaute-(III) trihydrate ($HAuCl_4 \cdot 3H_2O$, 99.99%), the stabilizing agents sodium citrate dihydrate (99%) and stearylamine (>80%), the reducing agent sodium borohydride ($NaBH_4$, 98%), and the solvents, ACS grade ethanol (95%) and toluene (99.7%), were purchased by VWR. Deuterium oxide (D_2O, 99.9%) was purchased from Cambridge Isotope Laboratories. The phospholipids 1,2-dipalmitoyl-*sn*-glycero-3-phosphocholine and 1,2-dipalmitoyl-*sn*-glycero-3-phospho-(1′-*rac*-glycerol) were purchased from Avanti Polar Lipids. All chemicals were used without further purification.

Nanoparticle Synthesis. Citrate-stabilized gold nanoparticles were prepared by a modified procedure similar to that of Jana *et al.*[26] In short, 30 mL of citrate solution (0.05 M) was added to 567 mL of DI water in a 1 L volumetric flask. Next, 3 mL of 0.05 M $HAuCl_4$ was added to the mixture and reduced with 3 mL of $NaBH_4$ (0.05 M). The resulting aqueous dispersed GNPs were ruby red in color.

The GNPs were resuspended in toluene by surface modification using stearylamine, similar to procedures previously

described.[27] Briefly, between 100 and 300 mL of 0.01 M stearylamine solutions in toluene were added to the 600 mL aqueous GNP dispersion in a volumetric flask. The biphasic mixture was vigorously shaken until the GNPs transferred from the aqueous phase to the toluene phase. The biphasic mixture was placed in a 1 L separatory funnel, where the toluene-dispersed GNPs were isolated from the aqueous phase. Next, ethanol was added to the GNPs (4:1 ethanol to GNP dispersion by volume) followed by centrifugation at 14 500 rpm for 10 min to induce nanoparticle precipitation. The supernatant liquid, containing excess stabilizing ligands and organic solvent, was decanted. The GNPs were resuspended in 20 mL neat solvent (hexane or toluene) followed by 5 min of sonication. The purification procedure was performed a total of three times before use.

Recursive fractionation using the antisolvent/solvent pair ethanol/toluene combined with centrifugation was performed as described by Korgel *et al.*[47] and White *et al.*[36] to isolate GNPs with a 3.9 nm core diameter using 40−45% ethanol antisolvent in toluene by volume. The synthesis, surface modification, and fractionation of GNPs were repeated until enough samples were prepared (nearly ∼30 mL at 5 mg/mL).

Lipid Vesicle Preparation. Vesicles were prepared at a DPPC/DPPG molar ratio of 85:15. For SANS the vesicles were prepared in D_2O, and for TEM and DSC they were prepared in deionized water. Vesicles were prepared at a sample volume of 1 mL using thin film hydration (TFH). Samples were prepared at 10 mM lipid for SANS and TEM and 0.1 mM for DSC. Preparation by TFH consisted of adding a chloroform/lipid solution to a round-bottom flask and evaporating the solvent using a rotary evaporator at 50 °C starting at 450 mbar for 30 min, then decreasing to 300 mbar for 30 min, and finally 200 mbar for 30 min. To remove the remaining solvent, the round-bottom flask containing the thin film was placed in a vacuum oven at room temperature for 2 h. To prepare GNP-loaded vesicles, GNPs in toluene were added to the lipid in chloroform before evaporation to yield *L*/*N* ratios from 10 000:1 to 5000:1. Water was added to the film at 50 °C, and the flask was hand shaken for 1 h followed by 30 min of bath sonication. The resulting aqueous dispersions were completely homogeneous, and no remaining precipitate was observed. On the basis of this observation, it is assumed that all of the hydrophobic nanoparticles were encapsulated within the vesicle bilayer. The samples were stored at 50 °C under a N_2 blanket prior to analysis.

Small-Angle Neutron Scattering. SANS experiments were performed on the CG-2 General SANS instrument at the High Flux Isotope Reactor at Oak Ridge National Laboratories (Oak Ridge, TN, USA). All samples were prepared to be 1% by volume and considered dilute. Each sample was loaded into a 2 mm path length banjo cell and measured at 25, 37, and 50 °C. Two sample-to-detector distances were used for the 25 and 37 °C measurements (0.3 and 6 m) to obtain a q range from ∼0.007 to 0.67 $Å^{-1}$ with a neutron wavelength of $\lambda = 6$ Å. An additional sample-to-detector distance of 14.5 m and a neutron wavelength of 18 Å were used for the 50 °C measurements to expand the q range to ∼0.001 $Å^{-1}$. The neutron resolutions, $\Delta\lambda/\lambda$, were equal to 12% (fwhm). Empty beam background, empty cell background, solvent (deuterium oxide) background, detector sensitivity, sample transmission, and sample thickness were considered during raw data reduction. The solvent and empty cell background measurements were used to normalize all SANS data. The reduced scattering intensities, $I(q)$, were fit as a function of the scattering vector, $q(\theta)$. Here, $q(\theta) = 4\pi \sin(\theta)/\lambda$, and θ is defined as the scattering angle. All SANS fitting was performed using Igor Pro 6.03 software and models provided by NIST.[40]

Transmission Electron Microscopy. TEM images of GNPs were obtained using a Hitachi 7600 with a 120 kV accelerating voltage. TEM samples were prepared by drop casting ∼5 μL of nanoparticle dispersion onto a 300-mesh Formvar carbon-coated copper TEM grid (Ted Pella), followed by solvent evaporation. The size distributions were obtained by image analysis performed with the ImageJ software package counting at least 1500 particles for meaningful and relevant statistics.

Cryo-TEM samples were prepared at 25 °C using a Vitrobot (FEI Company), which is a PC-controlled robot for sample vitrification. Quantifoil grids were used with 2 μm carbon holes on 200 square mesh copper grids (Electron Microscopy Sciences, Hatfield, PA, USA). To prepare a sample, it was first equilibrated within the Vitrobot at 25 °C and 100% humidity for 30 min. After immersing the grid into the sample, it was then removed, blotted to reduce film thickness, and vitrified in liquid ethane. The sample was then transferred to liquid nitrogen for storage. Imaging was performed in a cooled stage (model 915, Gatan Inc., Pleasanton, CA, USA) at 200 kV using a JEOL JEM-2100F TEM (Peabody, MA, USA).

Differential Scanning Calorimetry. DSC was performed using a TA Instruments Nano DSC (New Castle, DE, USA). Samples at 0.1 mM lipid were degassed under vacuum for 30 min before loading into a 0.6 mL capillary cell. The cell was then pressurized with nitrogen to 1 atm and equilibrated at 25 °C. Three consecutive heat/cool cycles were performed from 25 to 60 °C at a scan rate of 1 °C min^{-1}.

Conflict of Interest: The authors declare no competing financial interest.

Acknowledgment. This research was sponsored by the National Science Foundation (Grant Nos. EEC-082443 and CBET-0828022) and the National Institutes of Standards and Technology (Grant No. 60NANB10D139). Fellowship funding for G.V.W. at the time of this work was provided by the South East Alliance for Graduate Education and the Professoriate (SEAGEP) sponsored by the National Science Foundation (Grant No. HRD-0450279). A portion of this research was conducted at Oak Ridge National Laboratory's High Flux Isotope Reactor on the CG-3 Biological Small Angle Neutron Scattering (Bio-SANS) instrument, which is supported by the Scientific User Facilities Division, Office of Basic Energy Sciences, U.S. Department of Energy.

Supporting Information Available: Characterization of the nanoparticle ligand amount *via* TGA and further SANS analysis of the bilayer thickness are included. This material is available free of charge *via* the Internet at http://pubs.acs.org.

REFERENCES AND NOTES

1. Lu, X. M.; Rycenga, M.; Skrabalak, S. E.; Wiley, B.; Xia, Y. N. Chemical Synthesis of Novel Plasmonic Nanoparticles. *Ann. Rev. Phys. Chem.* **2009**, *60*, 167–192.
2. Wang, Z. X.; Ma, L. N. Gold Nanoparticle Probes. *Coord. Chem. Rev.* **2009**, *253*, 1607–1618.
3. Mirkin, C. A. The Polyvalent Gold Nanoparticle Conjugate-Materials Synthesis, Biodiagnostics, and Intracellular Gene Regulation. *MRS Bull.* **2010**, *35*, 532–539.
4. Talapin, D. V.; Lee, J. S.; Kovalenko, M. V.; Shevchenko, E. V. Prospects of Colloidal Nanocrystals for Electronic and Optoelectronic Applications. *Chem. Rev.* **2010**, *110*, 389–458.
5. Cortie, M. B.; McDonagh, A. M. Synthesis and Optical Properties of Hybrid and Alloy Plasmonic Nanoparticles. *Chem. Rev.* **2011**, *111*, 3713–3735.
6. McMahon, K. M.; Mutharasan, R. K.; Tripathy, S.; Veliceasa, D.; Bobeica, M.; Shumaker, D. K.; Luthi, A. J.; Helfand, B. T.; Ardehali, H.; Mirkin, C. A.; *et al.* Biomimetic High Density Lipoprotein Nanoparticles For Nucleic Acid Delivery. *Nano Lett.* **2011**, *11*, 1208–1214.
7. Osberg, K. D.; Schmucker, A. L.; Senesi, A. J.; Mirkin, C. A. One-Dimensional Nanorod Arrays: Independent Control of Composition, Length, and Interparticle Spacing with Nanometer Precision. *Nano Lett.* **2011**, *11*, 820–824.
8. Dickerson, E. B.; Dreaden, E. C.; Huang, X.; El-Sayed, I. H.; Chu, H.; Pushpanketh, S.; McDonald, J. F.; El-Sayed, M. A. Gold Nanorod Assisted Near-Infrared Plasmonic Photothermal Therapy (PPTT) of Squamous Cell Carcinoma in Mice. *Cancer Lett.* **2008**, *269*, 57–66.
9. Ding, H.; Yong, K.; Roy, I.; Pudavar, H. E.; Law, W. C.; Bergey, E. J.; Prasad, P. N. Gold Nanorods Coated with Multilayer Polyelectrolyte as Contrast Agents for Multimodal Imaging. *J. Phys. Chem. C* **2007**, *111*, 12552–12557.
10. Rosensweig, R. E. Heating Magnetic Fluid with Alternating Magnetic Field. *J. Magn. Magn. Mater.* **2002**, *252*, 370–374.

11. Bhattacharya, R.; Patra, C. R.; Earl, A.; Wang, S.; Katarya, A.; Lu, L.; Kizhakkedathu, J. N.; Yaszemski, M. J.; Greipp, P. R.; Mukhopadhyay, D.; *et al*. Attaching Folic Acid on Gold Nanoparticles using Noncovalent Interaction *via* Different Polyethylene Glycol Backbones and Targeting of Cancer Cells. *Nanomed.: Nanotechnol., Biol., Med.* **2007**, *3*, 224–38.
12. Urbina, M. C.; Zinoveva, S.; Miller, T.; Sabliov, C. M.; Monroe, W. T.; Kumar, C. S. S. R. Investigation of Magnetic Nanoparticle-polymer Composites for Multiple-Controlled Drug Delivery. *J. Phys. Chem. C* **2008**, *112*, 11102–11108.
13. Cabral, H.; Kataoka, K. Multifunctional Nanoassemblies of Block Copolymers for Future Cancer Therapy. *Sci. Technol. Adv. Mater.* **2010**, *11*, 014109.
14. Rasch, M. R.; Rossinyol, E.; Hueso, J. L.; Goodfellow, B. W.; Arbiol, J.; Korgel, B. A. Hydrophobic Gold Nanoparticle Self-Assembly with Phosphatidylcholine Lipid: Membrane-Loaded and Janus Vesicles. *Nano Lett.* **2010**, *10*, 3733–3739.
15. Ding, H.-m.; Tian, W.-d.; Ma, Y.-q. Designing Nanoparticle Translocation through Membranes by Computer Simulations. *ACS Nano* **2012**, *6*, 1230–1238.
16. Lund, T.; Callaghan, M. F.; Williams, P.; Turmaine, M.; Bachmann, C.; Rademacher, T.; Roitt, I. M.; Bayford, R. The Influence of Ligand Organization on the Rate of Uptake of Gold Nanoparticles by Colorectal Cancer Cells. *Biomaterials* **2011**, *32*, 9776–9784.
17. Chen, Y.; Bose, A.; Bothun, G. D. Controlled Release from Bilayer-Decorated Magnetoliposomes *via* Electromagnetic Heating. *ACS Nano* **2010**, *4*, 3215–3221.
18. Ahmed, S.; Madathingal, R. R.; Wunder, S. L.; Chen, Y. J.; Bothun, G. Hydration Repulsion Effects on the Formation of Supported Lipid Bilayers. *Soft Matter* **2011**, *7*, 1936–1947.
19. Park, S.; Oh, S.; Mun, J.; Han, S. Loading of Gold Nanoparticles inside the DPPC Bilayers of Liposome and Their Effects on Membrane Fluidities. *Colloids Surf., B* **2006**, *48*, 112–118.
20. Wijaya, A.; Hamad-Schifferli, K. High-Density Encapsulation of Fe_3O_4 Nanoparticles in Lipid Vesicles. *Langmuir* **2007**, *23*, 9546–9550.
21. Xia, T.; Rome, L.; Nel, A. Nanobiology: Particles Slip Cell Security. *Nat. Mater.* **2008**, *7*, 519–520.
22. Hossann, M.; Wang, T.; Wiggenhorn, M.; Schmidt, R.; Zengerle, A.; Winter, G.; Eibl, H.; Peller, M.; Reiser, M.; Issels, R. D.; Lindner, L. H. Size of Thermosensitive Liposomes Influences Content Release. *J. Controlled Release* **2010**, *147*, 436–443.
23. Amstad, E.; Kohlbrecher, J.; Muller, E.; Schweizer, T.; Textor, M.; Reimhult, E. Triggered Release from Liposomes through Magnetic Actuation of Iron Oxide Nanoparticle Containing Membranes. *Nano Lett.* **2011**, *11*, 1664–1670.
24. Katagiri, K.; Imai, Y.; Koumoto, K.; Kaiden, T.; Kono, K.; Aoshima, S. Magnetoresponsive On-Demand Release of Hybrid Liposomes Formed from Fe_3O_4 Nanoparticles and Thermosensitive Block Copolymers. *Small* **2011**, *7*, 1683–1689.
25. Al-Jamal, W. T.; Kostarelos, K. Liposomes: From a Clinically Established Drug Delivery System to a Nanoparticle Platform for Theranostic Nanomedicine. *Acc. Chem. Res.* **2011**, *44*, 1094–1104.
26. Bothun, G. D. Hydrophobic Silver Nanoparticles Trapped in Lipid Bilayers: Size Distribution, Bilayer Phase Behavior, and Optical Properties. *J. Nanobiotechnol.* **2008**, *6*.
27. Ivanova, V. P.; Makarov, I. M.; Schaffer, T. E.; Heimburg, T. Analyzing Heat Capacity Profiles of Peptide-Containing Membranes: Cluster Formation of Gramicidin A. *Biophys. J.* **2003**, *84*, 2427–2439.
28. Mouritsen, O. G.; Bloom, M. Mattress Model of Lipid-Protein Interactions in Membranes. *Biophys. J.* **1984**, *46*, 141–53.
29. Peschke, J.; Riegler, J.; Mohwald, H. Quantitative-Analysis of Membrane Distortions Induced by Mismatch of Protein and Lipid Hydrophobic Thickness. *Eur. Biophys. J. Biophys. Lett.* **1987**, *14*, 385–391.
30. Schmidt, U.; Guigas, G.; Weiss, M. Cluster Formation of Transmembrane Proteins due to Hydrophobic Mismatching. *Phys. Rev. Lett.* **2008**, *101*.
31. Huang, H. W.; Harroun, T. A.; Heller, W. T.; Weiss, T. M.; Yang, L. Experimental Evidence for Hydrophobic Matching and Membrane-mediated Interactions in Lipid Bilayers Containing Gramicidin. *Biophys. J.* **1999**, *76*, 937–945.
32. Heimburg, T.; Biltonen, R. L. A Monte Carlo Simulation Study of Protein-Induced Heat Capacity Changes and Lipid-Induced Protein Clustering. *Biophys. J.* **1996**, *70*, 84–96.
33. Jeng, U.-S.; Hsu, C.-H.; Lin, T.-L.; Wu, C.-M.; Chen, H.-L.; Tai, L.-A.; Hwang, K.-C. Dispersion of Fullerenes in Phospholipid Bilayers and the Subsequent Changes in the Host Bilayers. *Phys. B* **2005**, *357*, 193–198.
34. Jana, N. R.; Gearheart, L.; Murphy, C. J. Wet Chemical Synthesis of High Aspect Ratio Cylindrical Gold Nanorods. *J. Phys. Chem. B* **2001**, *105*, 4065–4067.
35. Liu, J.; Anand, M.; Roberts, C. B. Synthesis and Extraction of β-D-glucose-stabilized Au Nanoparticles Processed into Low-Defect, Wide-Area Thin Films and Ordered Arrays Using CO_2 Expanded Liquids. *Langmuir* **2006**, *22*, 3964–3971.
36. Von White, G.; Mohammed, F. S.; Kitchens, C. L. Small-Angle Neutron Scattering Investigation of Gold Nanoparticle Clustering and Ligand Structure Under Antisolvent Conditions. *J. Phys. Chem. C* **2011**, *115*, 18397–18405.
37. Nagle, J. F.; Tristram-Nagle, S. Structure of Lipid Bilayers. *Biochim. Biophys. Acta* **2000**, *1469*, 159–195.
38. Berghausen, J.; Zipfel, J.; Lindner, P.; Richtering, W. Influence of Water-Soluble Polymers on the Shear-Induced Structure Formation in Lyotropic Lamellar Phases. *J. Phys. Chem. B* **2001**, *105*, 11081–11088.
39. Kiselev, M. A.; Zemlyanaya, E. V.; Aswal, V. K.; Neubert, R. H. H. What Can We Learn About the Lipid Vesicle Structure from the Small-Angle Neutron Scattering Experiment? *Eur. Biophys. J. Biophys. Lett.* **2006**, *35*, 477–493.
40. Kline, S. R. Reduction and Analysis of SANS and USANS Data Using Igor Pro. *J. Appl. Crystallogr.* **2006**, *39*, 895–900.
41. Chen, Y.; Bothun, G. D. Cationic Gel-Phase Liposomes with "Decorated" Anionic SPIO Nanoparticles: Morphology, Colloidal, and Bilayer Properties. *Langmuir* **2011**, *27*, 8645–8652.
42. Troutier, A. L.; Veron, L.; Delair, T.; Pichot, C.; Ladaviere, C. New Insights into Self-Organization of a Model Lipid Mixture and Quantification of Its Adsorption on Spherical Polymer Particles. *Langmuir* **2005**, *21*, 9901–9910.
43. Kumar, A.; Mandal, S.; Selvakannan, P. R.; Pasricha, R.; Mandale, A. B.; Sastry, M. Investigation into the Interaction between Surface-bound Alkylamines and Gold Nanoparticles. *Langmuir* **2003**, *19*, 6277–6282.
44. Sastry, M.; Kumar, A.; Mukherjee, P. Phase Transfer of Aqueous Colloidal Gold Particles into Organic Solutions Containing Fatty Amine Molecules. *Colloids Surf., A* **2001**, *181*, 255–259.
45. Kralchevsky, P. A.; Paunov, V. N.; Denkov, N. D.; Nagayama, K. Stresses in Lipid-Membranes and Interactions between Inclusions. *J. Chem. Soc., Faraday Trans.* **1995**, *91*, 3415–3432.
46. Lee, C. H.; Lin, W. C.; Wang, J. P. All-Optical Measurements of the Bending Rigidity of Lipid-Vesicle Membranes across Structural Phase Transitions. *Phys. Rev. E* **2001**, *64*.
47. Korgel, B. A.; Fullam, S.; Connolly, S.; Fitzmaurice, D. Assembly and Self-organization of Silver Nanocrystal Superlattices: Ordered "Soft Spheres". *J. Phys. Chem. B* **1998**, *102*, 8379–8388.